



HAL
open science

Experimental study on the aeolotropic swelling behaviour of compacted bentonite/claystone mixture with axial/radial technological voids

Zhixiong Zeng, Yu-Jun Cui, Nathalie Conil, Jean Talandier

► To cite this version:

Zhixiong Zeng, Yu-Jun Cui, Nathalie Conil, Jean Talandier. Experimental study on the aeolotropic swelling behaviour of compacted bentonite/claystone mixture with axial/radial technological voids. *Engineering Geology*, 2020, 278, pp.105846. 10.1016/j.enggeo.2020.105846 . hal-03045823

HAL Id: hal-03045823

<https://enpc.hal.science/hal-03045823>

Submitted on 17 Oct 2022

HAL is a multi-disciplinary open access archive for the deposit and dissemination of scientific research documents, whether they are published or not. The documents may come from teaching and research institutions in France or abroad, or from public or private research centers.

L'archive ouverte pluridisciplinaire **HAL**, est destinée au dépôt et à la diffusion de documents scientifiques de niveau recherche, publiés ou non, émanant des établissements d'enseignement et de recherche français ou étrangers, des laboratoires publics ou privés.



Distributed under a Creative Commons Attribution - NonCommercial 4.0 International License

1 **Experimental study on the aeolotropic swelling behaviour of compacted**
2 **bentonite/claystone mixture with axial/radial technological voids**

3

4 Zhixiong Zeng^{1*}, Yu-Jun Cui¹, Nathalie Conil², Jean Talandier³

5

6 1: Ecole des Ponts ParisTech, Laboratoire Navier/CERMES, 6 et 8 avenue Blaise Pascal, 77455
7 Marne La Vallée cedex 2, France

8 2: Andra, Centre de Meuse/Haute-Marne, RD 960, 55290 Bure, France

9 3: Andra, 1/7, rue Jean Monnet, 92298 Châtenay-Malabry cedex, France

10

11

12

13

14

15 ***Corresponding author**

16 Zhixiong Zeng

17 Ecole des Ponts ParisTech

18 6–8 av. Blaise Pascal, Cité Descartes, Champs-sur-Marne

19 77455 Marne-la-Vallée cedex 2

20 France

21 Tel.: +33 781926608

22 Fax: +33 164153562

23 E-mail address: zhixiong.zeng@enpc.fr

24 **Abstract:** Pre-compacted blocks of MX80 bentonite/Callovo-Oxfordian (COx) claystone
25 mixture are chosen as sealing/backfilling materials in the French concept of deep geological
26 disposal for radioactive waste. Creating technological voids is normally unavoidable during
27 installation in the disposal galleries, in the form of axial voids between compacted blocks and
28 radial voids between the compacted blocks and the host rock. In this work, the aeolotropic
29 swelling behaviour of compacted mixture with axial/radial technological voids was
30 experimentally investigated. Results showed that the aeolotropy coefficient (ratio of radial to
31 axial pressures) of samples without voids increased from 0.46 to 0.88 with the increasing dry
32 density from 1.6 to 2.0 Mg/m³ due to the relatively concentrated macro-pores which defined a
33 relatively lower local dry density in the side part. For the samples with axial/radial voids, their
34 final axial swelling pressures were in agreement with the unique correlation with final dry
35 density, regardless of the soil density heterogeneity. Samples with axial voids had a larger
36 aeolotropy coefficient than samples without voids, due to the reduction of the orientation of clay
37 particles upon hydration, while samples with radial voids had a smaller aeolotropy coefficient, due
38 to the relatively lower dry density near the cell wall.

39 **Keywords:** bentonite/claystone mixture; axial/radial technological voids; swelling pressure;
40 aeolotropy coefficient

41 **1. Introduction**

42 In many countries, deep geological disposal has been considered as a possible solution to store
43 high-level radioactive wastes. (Pusch 1982; Sellin and Leupin 2013). In a promising concept, waste
44 canisters are emplaced within galleries excavated in a low-permeability formation a few hundred
45 metres below the surface. Bentonite-based materials are used to construct the sealing/backfilling
46 elements thanks to their favourable swelling characteristic, low permeability and good radionuclides
47 retention capacity (Dixon et al. 1985). A typical approach is to emplace bentonite-based materials in
48 the form of pre-compacted blocks between the host rock and waste canisters. Creating axial
49 technological voids between the compacted blocks, and radial technological voids between the
50 compacted blocks and the host rock is normally unavoidable during such installation operation.
51 After the disposal galleries are closed, the groundwater from the host rock will fill the technological
52 voids and progressively infiltrate into the bentonite-based materials. They swell and form a gel,
53 filling up the technological voids. Afterwards, swelling pressure develops progressively under
54 constrained volume condition. This swelling pressure must be high enough to limit the convergence
55 of the galleries in case of concrete lining failure (Cuisinier et al. 2008), but lower than the yield
56 stress supported by the sealing plugs (Saba et al. 2014a). It is therefore crucial to investigate the
57 swelling behaviour of compacted bentonite-based materials to achieve a reliable design of the
58 repository.

59 Numerous investigations have been carried out on the swelling behaviour of compacted
60 bentonite-based materials in the context of radioactive waste disposal (e.g. Komine and Ogata 1994,
61 1999; Cho et al. 2000; Lee et al. 1999; Saba et al. 2014a). It was well documented that the final
62 swelling pressure is dominated by bentonite dry density (Dixon et al. 1985; Lee et al. 1999; Wang et

63 [al. 2012](#)). However, the laboratory measurement of swelling pressure was generally carried out only
64 in the axial direction and the swelling pressures in different directions were considered as the same
65 in many cases. Recently, some researchers attempted to determine the difference between the
66 swelling pressures in different directions ([Lee et al. 2001, 2012](#); [Saba et al. 2014a](#); [Jia et al. 2019](#)).
67 [Lee et al. \(2012\)](#) measured both the axial and radial swelling pressures of compacted Korean
68 bentonite with a dry density of 1.5-1.7 Mg/m³ and observed a larger difference between the axial
69 and radial swelling pressures at a higher dry density. They attributed this phenomenon to the
70 fabrication process of compacted block, in which bentonite powders were uniaxially compacted. To
71 address this point, [Saba et al. \(2014a\)](#) defined an anisotropy coefficient as the ratio of radial to axial
72 swelling pressures. For compacted GMZ bentonite, [Jia et al. \(2019\)](#) found that the anisotropy
73 coefficient decreased from 1.0 to 0.76 owing to the increasingly oriented arrangement of bentonite
74 grains when the dry density increased from 1.46 to 1.71 Mg/m³. [Saba et al. \(2014a\)](#) studied the axial
75 and radial swelling pressures of compacted MX80 bentonite/sand mixture with a wide range of
76 bentonite dry density. They indicated that the anisotropy coefficient was mainly related to the
77 bentonite dry density: at low bentonite dry densities (lower than 1.16 Mg/m³), the anisotropy
78 decreased with increasing bentonite dry density; at medium dry densities (from 1.16 to 1.3 Mg/m³),
79 the coefficient was near 1.0; at high bentonite dry densities (larger than 1.3 Mg/m³), anisotropy
80 increased with increasing bentonite dry density. They explained this phenomenon by the swelling
81 and splitting of bentonite upon hydration, which could lead to microstructure collapse and thus
82 reduce the initial anisotropy induced by uniaxial compaction. At medium bentonite dry densities,
83 the microstructure collapse eliminated the initial anisotropy, developing an isotropic microstructure.
84 At high bentonite dry densities, the initial anisotropy would remain because the smaller macro-pore

85 space prevented the microstructure collapse. At very low dry densities, the macro-pores were not
86 fully filled by the swollen bentonite and the oriented microstructure was also preserved.

87 In the real deep geological repository, filling of technological voids will lead to a decrease in
88 the dry density of compacted blocks and the swelling behaviour can change upon hydration.
89 Moreover, the dry density distribution is not heterogeneous due to the presence of technological
90 voids in short term, influencing the swelling pressures in various directions. Many studies on the
91 swelling behaviour of compacted bentonite-based materials with technological voids were reported
92 (Villar et al. 2005; Saba et al. 2014a; Bian et al. 2019a, 2019b, 2020; Jia et al. 2019; Zeng et al.
93 2020a, 2020b, 2020c). Wang et al. (2013) and Saba et al. (2014a) pointed out that the unique
94 relationship between axial swelling pressure and final bentonite dry density could be extended to
95 compacted MX80 bentonite/sand mixture (70% bentonite-30% sand in dry mass) with 14% radial
96 technological voids. Moreover, Saba et al. (2014a) suggested that 14% radial technological voids
97 had a negligible effect on the anisotropy coefficient. Jia et al. (2019) performed several swelling
98 pressure tests on compacted GMZ bentonite with 13.3-26.7% axial voids. They concluded that a
99 void of more than 16.7% could induce a lower axial swelling pressure without significant change of
100 radial swelling pressure, resulting in an anisotropy coefficient higher than that without voids even
101 though the global dry density was the same. Their works were however limited to the voids between
102 compacted samples and the rigid cell wall, which simulated the host rock. The effect of axial
103 technological voids between the blocks was not studied. Moreover, the mechanism of swelling
104 behaviour of compacted blocks with axial/radial technological voids was not investigated.

105 This study investigated the aeolotropic swelling behaviour of compacted MX80
106 bentonite/Callovo-Oxfordian (COx) claystone mixture with technological voids. Unlike in Saba et

107 [al. \(2014a\)](#), the term of “aeolotropy” was adopted to distinguish from the common term of
108 “anisotropy”, which physically represents the intrinsic material property. To this end, the swelling
109 pressure of the samples was measured in both axial and radial directions by the constant-volume
110 method. Three set of experiments were performed to examine the effects of dry bulk density and
111 voids: (i) initial dry density varied without voids; (ii) final dry density varied using different initial
112 axial technological voids; (iii) final dry density varied using different initial radial technological
113 voids. After the swelling pressure tests, the water content and dry density at various positions were
114 determined to interpret the aeolotropic swelling mechanism of the compacted mixture with different
115 technological voids.

116 **2. Materials and methods**

117 *2.1. Materials*

118 The soil used in this study was a mixture of MX80 bentonite and crushed COx claystone (30/70 in
119 dry mass), which was selected as a candidate buffer/backfill material for the Cigéo project by the
120 French National Agency for Nuclear Waste Management (ANDRA). The MX80 bentonite was
121 extracted from Wyoming, USA. Its physical and mineralogical properties are presented in [Table 1](#).
122 The MX80 bentonite is of light gray colour, dominated by montmorillonite (86% in dry mass). The
123 liquid limit is 494%, the plastic limit is 46% and the unit mass is 2.76 Mg/m^3 , which are consistent
124 with the results of [Karnland et al. \(2008\)](#), [Tang et al. \(2008\)](#), [Seiphoori et al. \(2014\)](#) and [Saba et al.](#)
125 [\(2014\)](#). The crushed COx claystone used in this study was sampled from the ANDRA Underground
126 Research Laboratory (URL) in Bure. The COx claystone has an interstratified illite-smectite content
127 of 40-45% ([Fouché et al. 2004](#)) and a unit mass of 2.70 Mg/m^3 . The grain size distributions of the
128 bentonite and claystone powders determined by dry sieving and sedimentation ([ASTM D422, 2007](#))

129 are presented in Fig. 1. The D_{50} values of the dry bentonite and claystone powders are 0.55 and 0.58
130 mm, respectively. After saturation, the clay-size fractions of the bentonite and claystone are 86%
131 and 26%, respectively.

132 The saturation water used in this study was synthetic water prepared according to the methods
133 of Zeng et al. (2019).

134 2.2. Experimental technique and procedure

135 Fig. 2 depicts the experimental set-up used in this study. The test sample was installed in a stainless
136 cell (50 mm in diameter) and placed between two porous stones (hydraulic conductivity is about
137 1.0×10^{-5} m/s) and filter papers (hydraulic conductivity is about 0.15 m/s). It was saturated from the
138 bottom of the cell at a constant water pressure of 9.8 kPa and the expelled air/water flowed through
139 the air/water outlets at the top. The confined saturation conditions for the sample were guaranteed
140 by the cell wall and a metallic cap that was locked using a screw. A force transducer was mounted
141 under the cell base. A total pressure sensor (6 mm in diameter) was installed through a port on the
142 side of the cell and its measuring surface was flush with the cell wall to ensure satisfactory pressure
143 measurement. Based on the cell design, the axial force at the top of samples was transmitted to the
144 piston and then the force transducer while the total pressure sensor directly measured the radial
145 pressure at one location around the perimeter of the sample. All data were automatically collected
146 by a data logger. The whole set-up was placed in a constant temperature room (controlled at $20 \pm$
147 1 °C).

148 The soil was prepared by mixing the bentonite powder with claystone powder using a stirrer
149 for more than 10 min. The initial gravimetric water contents of the bentonite and claystone powders
150 were 11.4 and 6.1%, respectively. The water content of the obtained mixture was 7.7%. A

151 pre-determined amount of mixture was weighed and poured into a cylindrical mould. The samples
152 were prepared by compaction in the mould. Five disks (50 mm in diameter and 10 mm in height)
153 were compacted to the dry densities of 1.6, 1.7, 1.8, 1.9 and 2.0 Mg/m³, respectively, in order to
154 investigate the effect of dry density on the aeolotropic swelling behaviour (Table 2). Additionally,
155 another four disks at the same dimensions were compacted to a dry density of 2.0 Mg/m³ to study
156 the effect of radial voids. In the case of axial voids, twelve disks (49.80 mm in diameter and 5 mm
157 in height) with a dry density of 2.0 Mg/m³ were prepared.

158 For the tests without voids (T01 to 05), the samples were directly transferred into the test cell
159 by connecting the ends of the two cells (the compaction mould and test cell). For tests T06 to 09,
160 axial voids between the 5-mm disks were simulated by a pre-defined space between disks using
161 bentonite grains (Fig. 3a). For each test, three identical disks were used. After the installation of the
162 first disk, 0.10 g of bentonite grains of pre-defined sizes were scattered on the top of the disk. Then,
163 the second disk, the second layer of bentonite grains and the third disk were emplaced in sequence.
164 As a result, two identical layers of bentonite grains were sandwiched among three disks and two
165 gaps were created between disks. In this study, four samples with different gaps of 0.60, 0.80, 1.20
166 and 1.70 mm (corresponding to the technological voids of 7.4%, 9.6%, 13.8% and 18.5%,
167 respectively) were prepared using four groups of bentonite grains (0.25-0.40, 0.63-0.80, 1.00-1.25
168 and 1.60-2.00 mm). Note that the total mass of bentonite grains was smaller than 0.5% of all disks'
169 mass and thereby, their influence could be ignored. To facilitate the synthetic water to go into the
170 technological voids at the beginning of hydration, the lateral surfaces of all the disks were covered
171 by filter papers (about 0.10 mm thick), in addition to the filter papers at the top and bottom of
172 samples (Fig. 3a). For tests T10 to 13 (Fig. 3b), four compacted disks with a dry density of 2.0

173 Mg/m^3 were extracted from the compaction mould and trimmed into smaller disks with the same
174 height of 10 mm but with different diameters of 48.73, 47.43, 46.10 and 44.72 mm. The trimmed
175 disks were positioned at the centre of test cell, keeping the initial gaps of 5, 10, 15 and 20% of the
176 total volume respectively between the samples and cell wall. For all the tests (T01 to 13), the
177 pressure sensor corresponded to the middle position of samples by changing the thickness of the
178 porous stone at the bottom of samples. Note that for the tests with axial technological voids (T06 to
179 09), the testing surface of pressure sensor (6 mm in diameter) was in contact with the central disk (5
180 mm in thickness) and initial technological voids on the two sides of the central disk. Then, the
181 synthetic water was injected from the bottom of the cell and the axial and radial pressures were
182 measured during the hydration.

183 After the infiltration tests, the samples without voids (T01 to 05) and with radial voids (T10 to
184 13) were extracted from the cell by pushing the sample from the bottom. By contrast, for the tests
185 with axial voids (T06 to 09), the samples were carefully trimmed from the cell by cutting the edge
186 of sample, because the common extruding method may cause significant sample compaction and
187 lead to misjudgment on the soil density distribution in the vertical direction. The samples with
188 initial axial voids (T06 to 09) were divided into five parts termed part I, part II, part III, part IV and
189 part V, numbered sequentially from the top. As shown in [Fig. 4a](#), parts II and IV corresponded to
190 initial voids and a 1-mm thick surface disk from the two sides, while parts I, III and V were the
191 three disks. The sample T01 and those with initial radial voids (T10 to 13) were divided into parts I,
192 II and III. As shown in [Fig. 4b](#), part I is a ring having inner and outer diameters of 40 and 50 mm,
193 which included initial voids; part II is a ring with inner and outer diameters of 20 and 40 mm; part
194 III is the rest of the cylinder within a diameter of 20 mm. Each part was cut into two pieces. One

195 piece was oven-dried at 105 °C for a period of 24 h to determine the water content; the other piece
196 was immersed into non-aromatic hydrocarbon fluid (Kerdane) to determine the dry density.

197 **3. Experimental results**

198 *3.1. Swelling behaviour of samples without technological voids*

199 The evolutions of axial and radial swelling pressures with respect to elapsed time for the samples
200 without voids (T01 to 05) are shown in Fig. 5. Both axial and radial swelling pressures started with
201 a quick increase. For the samples with high dry densities (larger than 1.8 Mg/m³), the axial swelling
202 pressure increased and then reached stabilization at 5.18, 2.81 and 1.60 MPa after about 2600, 1860
203 and 1710 min for tests T01 to 03, respectively. For the samples with low dry densities (smaller than
204 1.7 Mg/m³), it increased until reaching peak values, then decreased and finally reached stabilization
205 at 0.83 and 0.46 MPa at about 1580 and 1060 min for T04 and T05, respectively. The times needed
206 to reach stabilization were comparable for the axial and radial swelling pressures. The final values
207 of swelling pressures are summarized in Table 2. The larger the dry density, the larger the final axial
208 and radial swelling pressures, in agreement with the observation by Zeng et al. (2019). Moreover,
209 the difference between them increased with the increase of dry density.

210 *3.2 Swelling behaviour of samples with axial technological voids*

211 The evolutions of axial and radial swelling pressures of samples T06 to 09 with different axial
212 technological voids are illustrated in Fig. 6. At the beginning of hydration, the axial swelling
213 pressure kept zero. After 5.4, 6.6, 12.0 and 28.8 min for tests T06 to 09, respectively, the axial
214 swelling pressure became measurable (Fig. 6a). With further hydration, the axial swelling pressure
215 increased and then tended to stabilize at 2.30, 1.59, 1.00 and 0.53 MPa after 2940, 2720, 2250 and
216 2120 min for tests T06 to 09, respectively. Overall, the larger the axial technological voids, the

217 lower the increasing rate. Unlike the axial swelling pressure, the radial swelling pressure started
218 with a quick increase at almost the same rate for tests T06 to 09. Subsequently, the radial swelling
219 pressure reached a peak value and then decreased. After about 390-min hydration, the radial
220 swelling pressures increased again and then reached stabilization values of 2.19, 1.53, 0.98 and 0.53
221 MPa after 2920, 2720, 2290 and 2060 min for tests T06 to 09, respectively. The final axial and
222 radial swelling pressures and the difference between them decreased with the increasing
223 technological voids.

224 At the end of tests, the samples were extracted from the cell and the dry density and water
225 content of different parts were determined. [Fig. 7](#) shows the distributions of dry density and water
226 content of samples. It appeared that the distributions of dry density and water content were
227 heterogeneous. Moreover, the larger the technological voids, the more heterogeneous the dry
228 density and water content distributions. Parts II and IV which included initial voids had a lower dry
229 density than the global one, whereas parts I, III and V had a higher dry density. The denser zone
230 (parts I, III and V) could undergo further swelling, while the looser zone (parts II and IV) would be
231 subjected to compression by the swelling pressure ([Bian et al. 2019a](#)). According to the measured
232 dry density and water content, the saturation degree of each part was calculated to be 98.6-104.4%
233 and the samples were almost saturated, confirming that no air was entrapped within the samples
234 after 10-day hydration.

235 *3.3. Swelling behaviour of samples with radial technological voids*

236 The evolutions of axial and radial swelling pressures of samples T10 to 13 with different radial
237 voids are depicted in [Fig. 8](#). The axial swelling pressure increased rapidly upon hydration. For tests
238 T10 and T11 (with less than 10% radial voids), the axial swelling pressure reached stabilization at

239 2.86 and 1.62 MPa after 500 and 440 min. For tests T12 and T13 (with more than 15% radial voids),
240 the axial swelling pressure increased and then reached the peak values of 0.97 and 0.80 MPa at 99
241 and 41 min, respectively. Afterwards, the axial swelling pressure tended to be stable at about 0.86
242 and 0.52 MPa after 410 and 400 min, respectively. Regarding the radial pressure, it kept zero during
243 the first 1.8, 4.8, 8.4 and 10.8 min of hydration for samples T10 to 13, respectively. After that, the
244 radial swelling pressure started to increase and then reached stabilization at 2.33, 1.14, 0.47 and
245 0.20 MPa after 480, 470, 460 and 400 min, respectively. On the whole, the increasing rate decreased
246 with the increasing technological voids. As the technological voids increased, the axial and radial
247 swelling pressures decreased, while the difference between them increased.

248 The dry density and water content profiles of samples T10 to 13 after infiltration tests are
249 depicted in Fig. 9. Heterogeneous distributions of dry density and water content were observed for
250 all the samples, with a lower dry density and higher water content in part I (looser) while a higher
251 dry density and lower water content in parts II and III (denser zone). This heterogeneity increased
252 with the increasing technological voids. According to the measured dry density and water content,
253 the saturation degree of each part was calculated and the calculated results varied from 98.4 to
254 101.5%, indicating that the samples were almost saturated even though the dry density distribution
255 was still heterogeneous.

256 **4. Interpretation and discussion**

257 *4.1. Swelling pressure kinetics*

258 As mentioned above, the swelling pressure kinetics of samples were highly dependent on the mode
259 and amount of technological voids. For the samples with axial technological voids (T06 to 09), the
260 axial voids were rapidly filled up by water with the help of lateral filter paper once the hydration

261 started. Then, the compacted disks swelled under free-swell condition in the axial direction and
262 under confined condition in the radial direction. The samples with different amount of axial voids
263 (T06 to 09) were under the same condition. Therefore, the axial pressure kept zero while the radial
264 one started with a quick increase at the same increasing rate until the adjacent disks came into
265 contact (Fig. 6a). Subsequently, the axial swelling pressure started to increase. However, the axial
266 swelling of the central disk (corresponding to the radial pressure sensor) simultaneously led to a
267 decrease in dry density in the vicinity of radial pressure sensor, resulting in a reduction of the radial
268 pressure. When this reduction induced by the axial swelling of the central disk was larger than the
269 increase of the radial swelling, peaks occurred on the radial swelling pressure curves (Fig. 6b). After
270 the axial voids were filled up by the swollen soils, the radial swelling pressure increased again and
271 then tended to stabilization. For the samples with radial technological voids (T10 to 13), the water
272 rapidly filled up the radial technological voids upon hydration, allowing the trimmed disk to imbibe
273 water from all the directions. In the axial direction, the axial swelling pressure increased quickly
274 while the soils swelled in the radial direction, filling the radial technological voids. Owing to the
275 significant radial swelling, a peak occurrence was identified on the axial swelling pressure curve of
276 samples with large radial technological voids (T12 and T13) (Fig. 8a). Once the radial technological
277 voids were filled by the swollen soils, the radial swelling pressure became measurable (Fig. 8b).
278 Afterwards, the samples imbibed water from the top and bottom, and tended to homogeneity.

279 To clarify the effect of technological voids on the swelling pressure kinetics of samples, the
280 evolutions of axial and radial swelling pressures of samples with the same initial dry density of 2.0
281 Mg/m³ (T01 and T06 to 13) are shown in Figs. 6 and 8. Additionally, the evolutions of axial and
282 radial swelling pressures of samples at a given global dry density (as an example, samples T03, T07

283 and T11 are selected and their global dry densities are 1.80, 1.81 and 1.80 Mg/m³, respectively) are
284 compared in Fig. 10. Compared to the samples without voids, a larger increasing rate of axial
285 swelling pressure was observed for the samples with radial voids at the beginning of hydration
286 while the samples with axial voids exhibited a lower one (Fig. 8a). This phenomenon could be
287 explained as follows. At the beginning of hydration, the samples with radial technological voids
288 were wetted from all the direction while the samples without voids were wetted only from the
289 bottom. As a result, the samples (T01 and T10 to T13) exhibited a similar increasing rate, regardless
290 of the radial technological voids. With further hydration, the radial voids would be filled by the
291 swollen soils, with a decrease of the dry density of compacted disk (T10 to T13) while the upper
292 layers of samples without voids (T01) were gradually hydrated by the synthetic water and swelled.
293 Hence, the increasing rate of axial swelling pressure for the sample without voids T01 became
294 larger than that of the samples with radial voids. For the samples with axial voids, the soils swelled
295 axially in volume at the beginning of hydration due to the presence of axial voids. Upon the filling
296 of axial voids, the samples absorbed water from the lateral sides, in addition to the top and bottom.
297 Therefore, a larger increasing rate was identified for the samples with axial voids compared to the
298 samples with radial voids at the same global dry density (water imbibition from the top and bottom),
299 as shown in Fig. 10a. As regards the radial pressure, even though the middle part of the sample
300 without voids could not significantly imbibe water from the bottom at a short time owing to the low
301 permeability of compacted disk, the middle part would be subjected to axial compression by the
302 lower layers through the K_0 effect (Saba et al. 2014c). This explained the rapid increase of radial
303 pressure (Figs. 6b and 8b), which accompanied the increasing axial swelling pressure. Owing to the
304 smaller distance to the water inlet, the radial pressure even exhibited a larger increasing rate than

305 the axial one, which was determined at the top of the samples (Fig. 2). For the samples with axial
306 voids, the pressure sensor was in contact with the central disk. Upon hydration, the central disk
307 swelled axially, filling the technological voids with a decreasing dry density of the compacted disk.
308 Thereby, a lower increasing rate of radial swelling pressure was observed, compared to the samples
309 without voids (Fig. 6b). For the samples with radial voids, the radial swelling pressure would be
310 measureable only after the filling of radial voids. This was why the samples with radial voids
311 exhibited the lowest increasing rate of radial swelling pressure (Fig. 10b).

312 4.2. Final axial and radial swelling pressures

313 4.2.1. Aeolotropic swelling pressure of samples without voids

314 In addition to the swelling pressure kinetics, the final swelling pressures of samples are of equal
315 importance. Fig. 11 shows the relationships between the final axial and radial swelling pressures
316 and the global dry density for the samples without voids. The logarithm of axial and radial swelling
317 pressures increased linearly with the increasing dry density. The relationships between the final
318 axial swelling pressure ($P_{s\text{-axial}}$ in MPa), the final radial swelling pressure ($P_{s\text{-radial}}$ in MPa) and the
319 dry density (ρ_d in Mg/m^3) for the samples without voids could be described by unique correlations
320 with squared correlation coefficients of 0.999:

$$321 \quad P_{s\text{-axial}} = 2.030 \times 10^{-3} \rho_d^{11.313} \quad (1)$$

$$322 \quad P_{s\text{-radial}} = 5.112 \times 10^{-4} \rho_d^{13.122} \quad (2)$$

323 From Fig. 11, it could also be observed that the axial swelling pressure was larger than the radial
324 one. To further analyse this aeolotropic behaviour, the ratio of measured radial to axial swelling
325 pressures, which was termed as aeolotropy coefficient, for all the samples was calculated. The
326 relationship between the aeolotropy coefficient and global dry density for the samples without voids

327 is shown in Fig. 12. It appears that the aeolotropy coefficient increased from 0.46 to 0.88 as the dry
328 density increased from 1.6 to 2.0 Mg/m³. Similar experimental studies were conducted on
329 compacted pure Korean bentonite with dry densities ranging from 1.5 to 1.7 Mg/m³ by Lee et al.
330 (2012) and on compacted MX80 bentonite/sand mixture (70/30 in dry mass) with bentonite dry
331 densities from 0.94 to 1.45 Mg/m³ by Saba et al. (2014a). With the increase of dry density, the
332 aeolotropy coefficient increased until reaching a peak value at the turning point and then decreased
333 (Fig. 13). This phenomenon could be due to the combined effects of the heterogeneous distribution
334 of macro-pores in the radial direction and the oriented arrangement of grains (Fig. 14). When grains
335 with a dimension significantly larger than others were poured in the compaction mould, they would
336 favour an oriented arrangement with a larger face side in the horizontal direction, as shown by Saba
337 (2013) in a quantitative study. Additionally, more macro-pores could exist in the side part of
338 samples due to the friction between grains and the mould wall, which was verified by Saba et al.
339 (2014b) and Than et al. (2016) through X-ray computed tomography (μ CT). Both of them would
340 lead to an aeolotropic swelling behaviour upon hydration. During the subsequent compaction
341 process, the oriented arrangement of grains increased with the increasing dry density while the
342 heterogeneity of macro-pores would be reduced because of the squeeze of small grains into the side
343 part (Than et al. 2016). Fig. 15 shows a sketch of compacted bentonite (various dry densities)
344 before and after saturation. For the samples at low dry densities, the bentonite grains swelled and
345 split up, but they could not fill up the macro-pores, especially at the side part. As shown in Fig. 2,
346 the pressure sensor in contact with the side part of samples measured a lower radial swelling
347 pressure when there were more macro-pores present in this zone (Fig. 15a), giving rise to a lower
348 aeolotropy coefficient. For the samples at high dry densities, the grains could not fully swell due to

349 the limited macro-pores between grains (Fig. 15c). Thus, the initial orientation would be preserved.

350 For the samples at medium dry densities, the bentonite grains could swell and well fill the

351 macro-pores (Fig. 15b), resulting in a relatively isotropic behaviour. Summarizing, the aeolotropic

352 swelling behaviour for the samples at low dry densities could be mainly attributed to the

353 heterogeneous distribution of macro-pores in the radial direction while the influence of grain

354 orientation became dominant when the dry density of samples was larger than the turning point.

355 Obviously, the swelling capacity of bentonite governed the filling process of macro-pores,

356 influencing the turning point. Because of the lower montmorillonite content of Korean bentonite

357 (70%) as compared with that of MX80 bentonite (86%), a larger turning point was observed for the

358 Korean bentonite (Fig. 13). Furthermore, this turning point was also dependent on the property of

359 studied material such as grain size and water content. For the sample with a larger size and lower

360 water content, more macro-pores could be present in the side part owing to the larger friction with

361 the mould wall. In that case, a larger turning point could be expected. In this work, the used material

362 was a MX80 bentonite/COx claystone mixture with a claystone fraction as large as 70%. As the

363 grain size of COx claystone was larger than that of MX80 bentonite while its water content was

364 lower than that of MX80 bentonite, a higher concentration of macro-pores in the side parts could be

365 expected in this bentonite/claystone mixture. Additionally, the swelling capacity of this mixture was

366 quite low because the swelling capacity of major claystone is lower than 1% of that of bentonite

367 (Zeng et al. 2019). Therefore, the heterogeneity of macro-pores in the radial direction was difficult

368 to eliminate after hydration and a large turning point was obtained for this mixture. For the samples

369 with dry densities ranging from 1.6 to 2.0 Mg/m³, their aeolotropic swelling behaviour would be

370 mainly influenced by the heterogeneity of macro-pores and only the increasing trend of aeolotropy

371 coefficient with the increasing dry density was observed.

372 4.2.2. Aeolotropic swelling pressure of samples with axial/radial voids

373 As far as the effect of technological voids was concerned, their presence led to the decreases of
374 axial and radial swelling pressures (Table 2). The variations of the axial swelling pressure with the
375 global dry density for the samples with axial/radial voids are also presented in Fig. 11. It could be
376 observed that the axial swelling pressure for samples with axial/radial voids were in satisfactory
377 agreement with that of samples without voids. This good agreement indicted that the final axial
378 swelling pressure of compacted disks were mainly dependent on the global dry density, irrespective
379 of the heterogeneity due to the presence of technological voids and the mode of voids (axial/radial
380 voids). The variation in the radial swelling pressure with dry density for the samples with radial
381 voids and without voids is also illustrated in Fig. 11. For samples with axial voids, since the dry
382 density distribution was heterogeneous along the sample height at the end of infiltration tests, the
383 distribution of radial swelling pressure was expected to be non-uniform. As the pressure sensor was
384 located at the middle of the samples and in contact with parts II, III and IV, and the areas of contact
385 between the pressure sensor and parts II, III and IV (A_2 , A_3 and A_4) were 5.23, 17.22 and 5.23 mm²,
386 the average dry density of soils ($\rho_{d\text{-sensor}}$ in Mg/m³) in contact with the pressure sensor could be
387 calculated using Eq. (3):

$$388 \quad \rho_{d\text{-sensor}} = (\rho_{d\text{-II}} \times A_2 + \rho_{d\text{-III}} \times A_3 + \rho_{d\text{-IV}} \times A_4) / (A_2 + A_3 + A_4) \quad (3)$$

389 where $\rho_{d\text{-II}}$, $\rho_{d\text{-III}}$, $\rho_{d\text{-IV}}$ are the dry density of parts II, III and IV, respectively. The values of average
390 dry density were calculated to be 1.87, 1.81, 1.74 and 1.64 Mg/m³, for tests T06-09, respectively.
391 Thereby, the radial swelling pressure versus the average soil dry density near the pressure sensor is
392 shown in Fig. 11. It appears that the samples with axial voids exhibited a larger radial swelling

393 pressure than those without voids at the same dry density, while the samples with radial voids
394 showed a lower one, especially for those with more than 15% radial voids. The aeolotropy
395 coefficients of the samples with axial/radial voids are also summarized in Fig. 12. Note that the
396 aeolotropy coefficient for the samples with axial voids was determined according to the axial and
397 radial swelling pressures of soils in the vicinity of the pressure sensor. The axial swelling pressures
398 of soils in contact with the pressure sensor were estimated using Eq. (1). From Fig. 12, the samples
399 with axial voids exhibited a larger aeolotropy coefficient than those without voids, whereas the
400 samples with radial voids showed a lower one, albeit at the same dry density. The aeolotropic
401 swelling mechanism of the compacted bentonite/claystone mixture with axial/radial voids is shown
402 in Fig. 16. Upon hydration, the clay particles of the samples with axial voids swelled and split up,
403 filling up the initial axial voids. This process allowed the rearrangement of clay particles and
404 reduced the initial orientation of clay particles (Fig. 16a). Consequently, a less aeolotropic
405 behaviour was observed for the samples with axial voids. Furthermore, larger axial voids would
406 provide more spaces for the swelling of clay particles, leading to more pronounced reductions in the
407 orientation of clay particles. This explained why the aeolotropy coefficient increased with the
408 increasing axial technological voids (decreasing dry density). When the radial technological voids
409 were considered, the radial sensor was in contact with the soils in the side part (part I) where the dry
410 density was lower than the global one (Fig. 16b) and the measured radial swelling pressure was
411 lower than that of samples without voids, especially for the samples with more than 15% voids (Fig.
412 11). As shown in Fig. 10a, the larger initial voids, the more heterogeneous the dry density
413 distribution. Hence, a larger reduction in the aeolotropy coefficient was observed for the samples
414 with larger initial radial voids. In other words, radial voids would increase the heterogeneity of dry

415 density in the radial direction, giving rise to a more pronounced aeolotropic behaviour; by contrast,
416 the axial voids could decrease the initial orientation of clay particles, leading to a less pronounced
417 aeolotropic behaviour.

418 As remarked above, the dry density distributions of samples with axial/radial voids were
419 non-uniform at the end of infiltration tests. Over time, the soils in the looser zone would be
420 compressed by swelling pressure with an increase in dry density, whereas the soils in the denser
421 zone underwent further swelling with a decrease in dry density, resulting in a relatively
422 homogenous distribution. For the samples with axial technological voids, the swollen clay particles
423 would become more oriented under the swelling pressure, leading to a decrease of aeolotropy
424 coefficient. For the samples with radial voids, this homogenization process would reduce the
425 concentration of macro-pores in the side part, resulting in an increase of aeolotropy coefficient.
426 However, the dry density gradient could remain for longtime because of the friction between the
427 samples and cell wall. To this end, the samples with axial voids would present a relatively higher
428 aeolotropy coefficient in long term than those without voids whereas the samples with radial voids
429 would show a lower one.

430 **5. Conclusions**

431 Constant-volume swelling pressure tests were performed on compacted MX80 bentonite/COx
432 claystone mixture at different dry densities and the swelling pressures in both axial and radial
433 directions were obtained, allowing the effect of dry density on the aeolotropic swelling behaviour to
434 be determined. To study the effects of axial/radial voids on the aeolotropic swelling behaviour,
435 swelling pressures of the samples with different axial/radial technological voids were measured,
436 together with the determination of dry density and water content at different positions. From the

437 experimental results, the following conclusions can be drawn.

438 The axial swelling pressure was dominated by global dry density, regardless of the presence of
439 technological voids and the mode of technological voids (axial or radial voids). At the same dry
440 density, the samples with axial technological voids had a larger radial swelling pressure than those
441 without voids while the samples with radial voids exhibited a smaller one, especially for the
442 samples with larger voids.

443 For the samples without voids, the aeolotropy coefficient (ratio of radial to axial swelling
444 pressures) increased and then decreased with the increasing dry density due to the combined effects
445 of the concentration of macro-pores in the border of samples and the orientation of clay particles. At
446 low dry densities, the swelling aeolotropy was mainly conditioned by the former. As the dry density
447 decreased, the heterogeneous distribution of macro-pores decreased while grain orientation
448 increased. Therefore, the swelling aeolotropy was dominated by the latter, in case of high dry
449 densities.

450 At the same dry density, the samples with axial voids exhibited a larger aeolotropy coefficient
451 than those without voids, thanks to the reductions of the orientation of clay particles. On the
452 contrary, the samples with radial voids presented a lower one because of the lower dry density in the
453 side part. Furthermore, the larger the technological voids, the more significant the influence of
454 axial/radial voids on the aeolotropic swelling behaviour.

455

456 **Acknowledgments**

457 The authors are grateful to Ecole des Ponts ParisTech and the French National Agency for Nuclear
458 Waste Management (ANDRA). The first author also wishes to acknowledge the support of the

459 China Scholarship Council (CSC).

460

461 **References**

462 American Society for Testing and Materials (ASTM), 2007. Standard Test Method for Particle-Size
463 Analysis of Soils. Soil and Rock, West Conshohocken, PA. D422.

464 Bian, X., Cui, Y.J., and Li, X.Z., 2019a. Voids effect on the swelling behaviour of compacted
465 bentonite. *Géotechnique*, 69(7): 593-605.

466 Bian, X., Cui, Y.J., Zeng, L.L. and Li, X.Z., 2019b. Swelling behavior of compacted bentonite with
467 the presence of rock fracture. *Engineering Geology*, 254: 25-33.

468 Bian, X., Cui, Y.J., Zeng, L.L. and Li, X.Z., 2020. State of compacted bentonite inside a fractured
469 granite cylinder after infiltration. *Applied Clay Science*. doi: 10.1016/j.clay.2020.105438.

470 Cho, W.J., Lee, J.O., Kang, C.H., 2000. Influence of temperature elevation on the sealing
471 performance of a potential buffer material for a high-level radioactive waste repository. *Annals*
472 *of Nuclear Energy*, 27(14), 1271-1284.

473 Dixon, D.A., Gray, M.N., Thomas, A.W., 1985. A study of the compaction properties of potential
474 clays and buffer mixtures for use in nuclear fuel waste disposal. *Eng. Geol.* 21(3/4):247-255.

475 Jia, L.Y., Chen, Y.G., Ye, W.M., Cui, Y.J. 2019. Effects of a simulated gap on anisotropic swelling
476 pressure of compacted GMZ bentonite. *Engineering geology*, 248: 155-163.

477 Karnland, O., Nilsson, U., Weber, H., Wersin. P., 2008. Sealing ability of Wyoming bentonite
478 pellets foreseen as buffer material–laboratory results. *Phys. Chem. Earth Parts A/B/C.* 33,
479 S472-S475.

480 Komine, H., Ogata, N., 1994. Experimental study on swelling characteristics of compacted
481 bentonite. *Can. Geotech. J.* 31(4), 478-490.

482 Komine, H., Ogata, N., 1999. Experimental study on swelling characteristics of sand-bentonite
483 mixture for nuclear waste disposal. *Soils Found.* 39(2), 83-97.

484 Lee, J.O., Cho, W.J., Chun, K.S., 1999. Swelling pressures of a potential buffer material for
485 high-level waste repository. *J. Korean Nucl. Soc.* 31(2), 139-150.

486 Lee, J.O., Cho, W.J., Kang, C.H., Chun, K.S., 2001. Swelling and hydraulic properties of
487 Ca-bentonite for the buffer of a waste repository (No. IAEA-CSP--6/C).

488 Lee, J.O., Lim, J.G., Kang, I.M., Kwon, S., 2012. Swelling pressures of compacted Ca-bentonite.
489 Engineering Geology, 129, 20-26.

490 Pusch, R., 1982. Mineral–water interactions and their influence on the physical behavior of highly
491 compacted Na bentonite. Can. Geotech. J. 19(3), 381-387.

492 Saba, S., 2013. Hydro-mechanical behaviour of bentonite-sand mixture used as sealing materials in
493 radioactive waste disposal galleries (Doctoral dissertation, Université Paris-Est).

494 Saba, S., Barnichon, J. D., Cui, Y. J., Tang, A. M., Delage, P., 2014a. Microstructure and
495 anisotropic swelling behaviour of compacted bentonite/sand mixture. J. Rock Mech. Geotech.
496 Eng. 6(2), 126-132.

497 Saba, S., Delage, P., Lenoir, N., Cui, Y.J., Tang, A.M., Barnichon, J.D., 2014b. Further insight into
498 the microstructure of compacted bentonite–sand mixture. Engineering geology, 168, 141-148.

499 Saba, S., Cui, Y.J., Tang, A.M., Barnichon, J.D., 2014c. Investigation of the swelling behaviour of
500 compacted bentonite–sand mixture by mock-up tests. Canadian geotechnical journal, 51(12),
501 1399-1412.

502 Seiphoori, A., Ferrari, A., Laloui. L., 2014. Water retention behaviour and microstructural evolution
503 of MX-80 bentonite during wetting and drying cycles. Géotechnique. 64(9), 721-734.

504 Sellin, P., Leupin, O.X., 2013. The use of clay as an engineered barrier in radioactive-waste
505 management—a review. Clays Clay Miner. 61(6), 477-498.

506 Tang, A.M., Cui, Y.J., Le, T.T., 2008. A study on the thermal conductivity of compacted bentonites.
507 Appl. Clay Sci. 41(3-4), 181–189.

508 Than, V.D., Aïmediou, P., Pereira, J.M., Roux, J.N., Bornert, M., Tang, A.M., 2016.
509 Macro-microscopic one-dimensional compression of wet granular soils by experimental
510 investigation. E3S Web of Conferences.

511 Villar, M.V., García-Siñeriz, J.L., Bárcena, I., Lloret, A., 2005. State of the bentonite barrier after
512 five years operation of an in situ test simulating a high level radioactive waste repository.
513 Engineering Geology, 80(3-4), 175-198.

514 Wang, Q., Tang, A.M., Cui, Y.J., Delage, P., Gatmiri, B., 2012. Experimental study on the swelling
515 behaviour of bentonite/claystone mixture. Eng. Geol. 124, 59-66.

516 Wang, Q., Tang, A.M., Cui, Y.J., Delage, P., Barnichon, J.D., Ye, W.M., 2013. The effects of
517 technological voids on the hydro-mechanical behaviour of compacted bentonite–sand mixture.

518 Soils and Foundations, 53(2), 232-245.

519 Zeng, Z.X., Cui, Y.J., Zhang, F., Conil, N., Talandier, J., 2019. Investigation of swelling pressure of
520 bentonite/claystone mixture in the full range of bentonite fraction. Applied Clay Science. doi:
521 10.1016/j.clay.2019.105137.

522 Zeng, Z.X., Cui, Y.J., Zhang, F., Conil, N., Talandier, J., 2020a. Effect of technological voids on
523 the swelling behaviour of compacted bentonite/claystone mixture. Can. Geotech. J.
524 <https://doi.org/10.1139/cgj-2019-0339>.

525 Zeng, Z.X., Cui, Y., Conil, N. Talandier J., 2020b. Analysis of boundary friction effect on the
526 homogenization process of compacted bentonite/claystone mixture with technological voids
527 upon hydration. Acta Geotech. <https://doi.org/10.1007/s11440-020-01048-x>.

528 Zeng, Z.X., Cui, Y.J., Conil, N., Talandier, J., 2020c. Effects of technological voids and hydration
529 time on the hydro-mechanical behaviour of compacted bentonite/claystone mixture.
530 Géotechnique. <https://doi.org/10.1680/jgeot.19.P.220>.

531	List of Tables
532	Table 1 Physical and mineralogical properties of MX80 bentonite
533	Table 2 Experimental program and main results
534	List of Figures
535	Fig. 1 Grain size distribution of MX80 bentonite and crushed COx claystone
536	Fig. 2 Layout of the constant-volume cell
537	Fig. 3 Different technological voids considered: (a) axial voids and (b) radial voids
538	Fig. 4 Schematic view of sample cutting: (a) axial voids and (b) radial voids
539	Fig. 5 Evolutions of axial and radial swelling pressures of samples without voids: (a) axial swelling
540	pressure and (b) radial swelling pressure
541	Fig. 6 Evolutions of axial and radial swelling pressures of samples with axial voids: (a) axial
542	swelling pressure and (b) radial swelling pressure
543	Fig. 7 Dry density and water content profiles for the samples with axial voids: (a) dry density and (b)
544	water content. Note: the dash lines in the left graph represent the global dry density calculated using
545	the total volume after filling technological voids instead of initial state while the dash lines in the
546	right graph refer to the global water content corresponding to the global dry density and a 100%
547	degree of saturation
548	Fig. 8 Evolutions of axial and radial swelling pressures of samples with radial voids: (a) axial
549	swelling pressure and (b) radial swelling pressure
550	Fig. 9 Dry density and water content profiles for sample T01 and those with radial voids (T10 to13):
551	(a) dry density and (b) water content. Note: the dash lines in the left graph represent the global dry
552	density calculated using the total volume after filling technological voids instead of initial state
553	while the dash lines in the right graph refer to the global water content corresponding to the global
554	dry density and a 100% degree of saturation
555	Fig. 10 Comparison of the swelling pressure kinetics of samples in different cases: (a) axial
556	swelling pressure and (b) radial swelling pressure
557	Fig. 11 Relationship between axial and radial swelling pressures and dry density
558	Fig. 12 Relationship between aeolotropy coefficient and dry density of bentonite/claystone mixture.
559	Note: the aeolotropy coefficient of the samples with axial voids was determined according to the
560	axial and radial swelling pressures of the soils in contact with the pressure sensor
561	Fig. 13 Aeolotropy coefficient changes with bentonite dry density for different bentonites (data
562	from Lee et al. (2012) and Saba et al. (2014a))
563	Fig. 14 Representation of the effects of grain orientation and concentrated macro-pores in the side
564	part. Note: the curves in the figure are schematically drawn and do not represent measured values
565	Fig. 15 Schematic view of aeolotropic swelling mechanism in compacted bentonite at: (a) low dry

566 densities; (b) medium dry densities; (c) high dry densities

567 Fig. 16 Schematic view of aeolotropic swelling mechanism in compacted bentonite/claystone

568 mixture with: (a) axial voids; (b) radial voids

Table 1 Physical and mineralogical properties of MX80 bentonite

Soil property	This work	Tang et al. (2008)	Seiphoori et al. (2014)	Saba et al. (2014)	Karland et al. (2008)
Specific gravity	2.76	2.76	2.74	2.77	-
Consistency limit					
Liquid limit (%)	494	520	420	575	-
Plastic limit (%)	46	42	65	53	-
Plasticity index (%)	448	478	355	522	-
Main minerals					
Montmorillonite (%)	86	92	85	-	80
Quartz (%)	7	3	-	-	2-3

Table 2 Experimental program and main results

Test No.	Technological voids		Global dry density (Mg/m ³)	Final axial swelling pressure (MPa)	Final lateral swelling pressure (MPa)
	Mode	Amount (%)			
T01	Without	0	2.0	5.18	4.55
T02	voids	0	1.90	2.81	2.35
T03		0	1.80	1.60	1.14
T04		0	1.70	0.83	0.53
T05		0	1.60	0.46	0.21
T06		Axial	7.4	1.85	2.30
T07	voids	9.6	1.81	1.59	1.53
T08		13.8	1.72	1.00	0.98
T09		18.5	1.63	0.53	0.53
T10	Radial	5	1.90	2.86	2.33
T11	voids	10	1.80	1.62	1.14
T12		15	1.70	0.86	0.47
T13		20	1.60	0.52	0.20

573
574

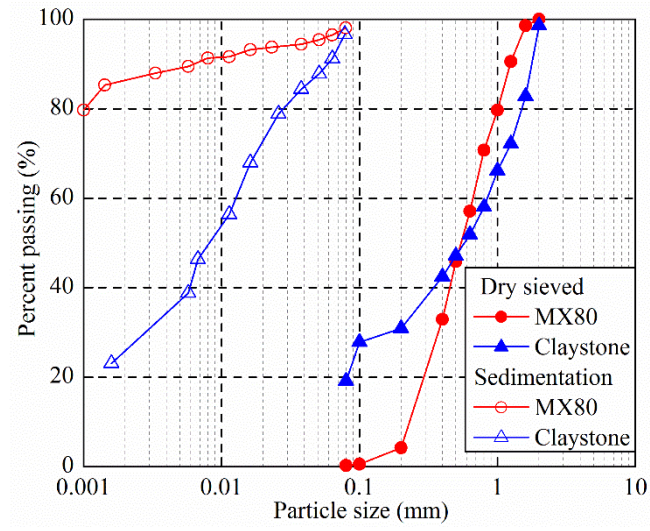


Fig. 1 Grain size distributions of MX80 bentonite and crushed COx claystone

575
576

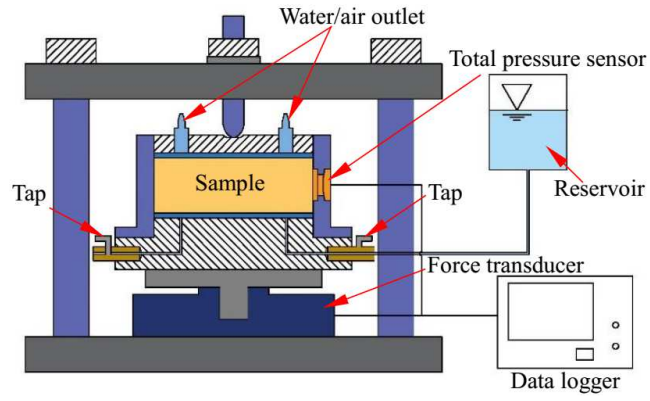
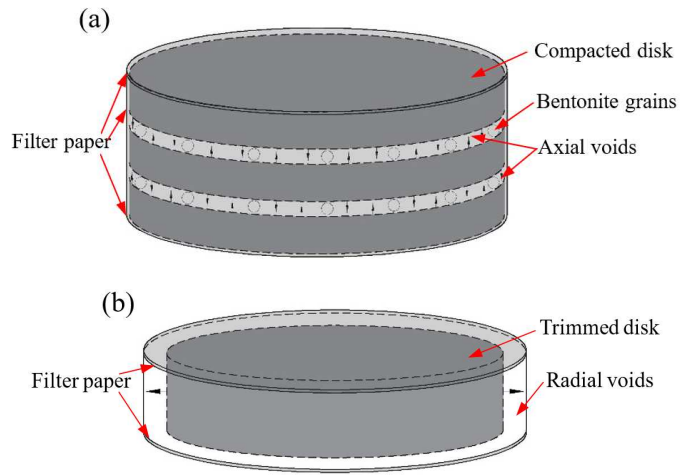


Fig. 2 Layout of the constant-volume cell



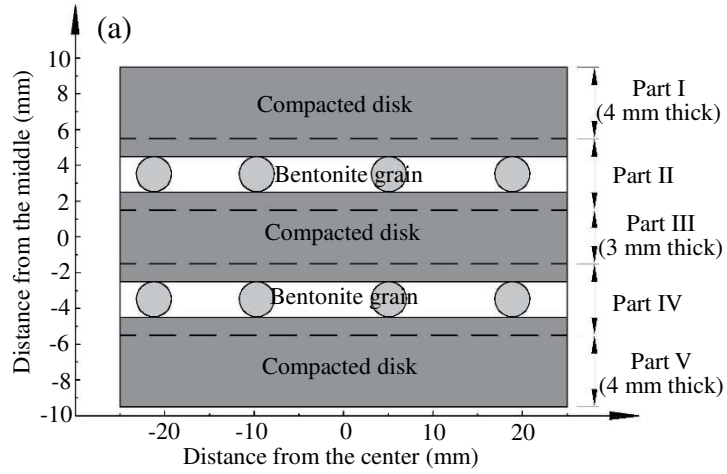
577

578

579

Fig. 3 Different technological voids considered: (a) axial voids and (b) radial voids

580



581

582

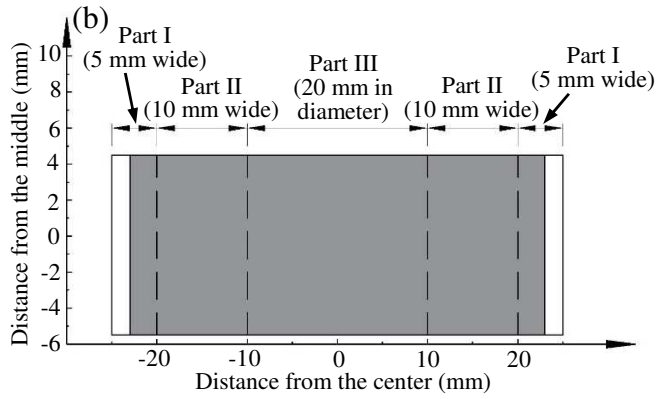
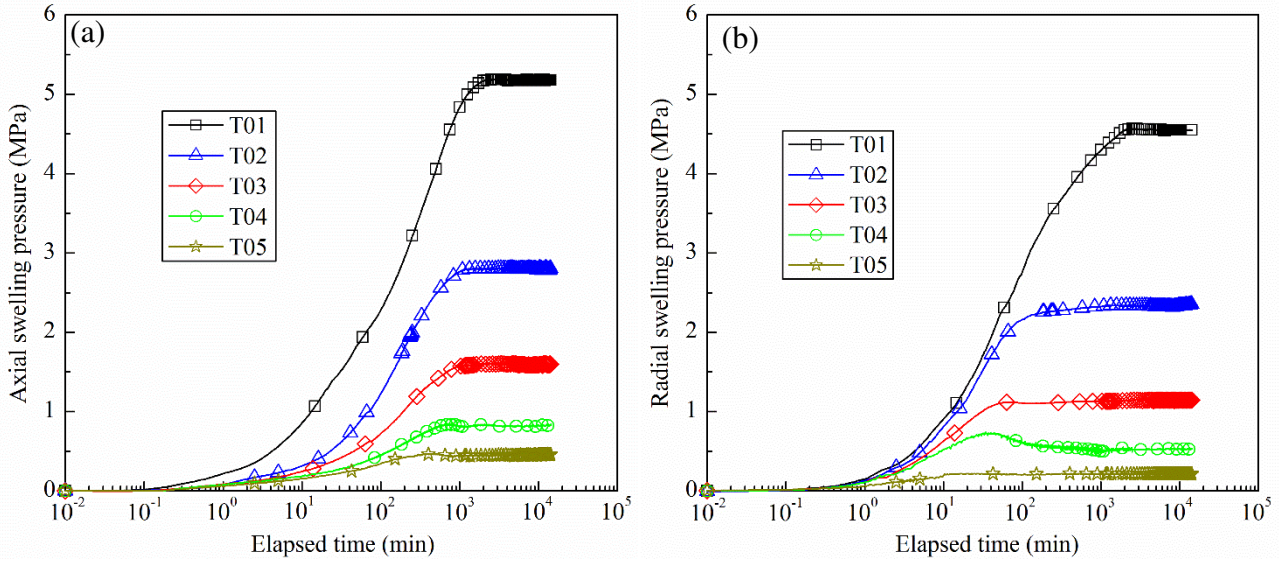


Fig. 4 Schematic view of sample cutting: (a) axial voids and (b) radial voids



583
584
585

Fig. 5 Evolutions of axial and radial swelling pressures of samples without voids: (a) axial swelling pressure and (b) radial swelling pressure

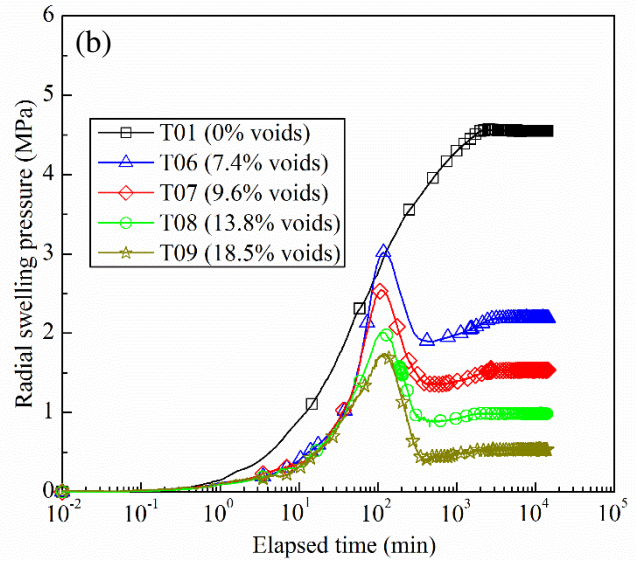
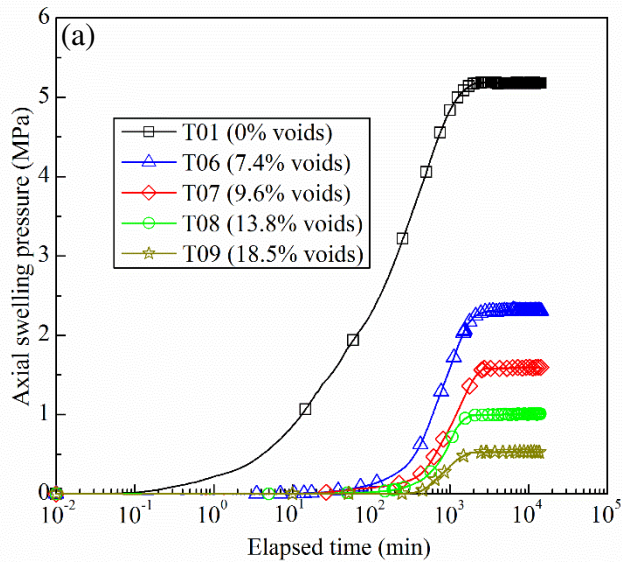
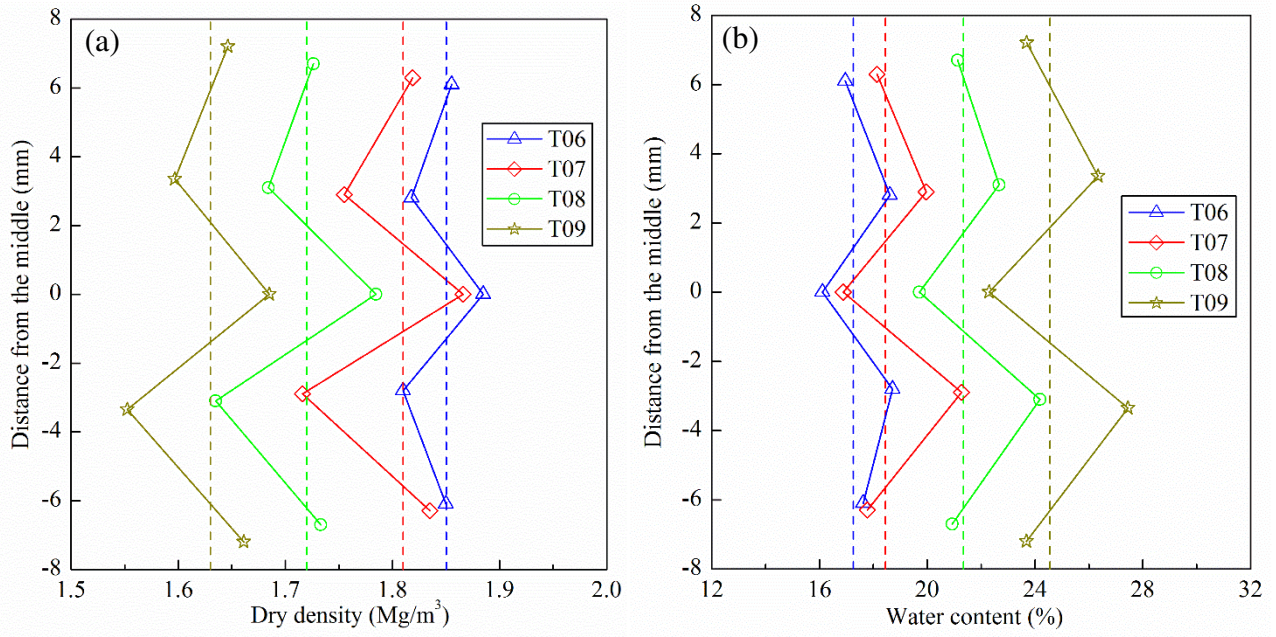


Fig. 6 Evolutions of axial and radial swelling pressures of samples with axial voids: (a) axial swelling pressure and (b) radial swelling pressure

586
587
588



589
 590 **Fig. 7** Dry density and water content profiles for the samples with axial voids: (a) dry density and (b) water content. Note: the dash
 591 lines in the left graph represent the global dry density calculated using the total volume after filling technological voids instead of
 592 initial state while the dash lines in the right graph refer to the global water content corresponding to the global dry density and a 100%
 593 degree of saturation

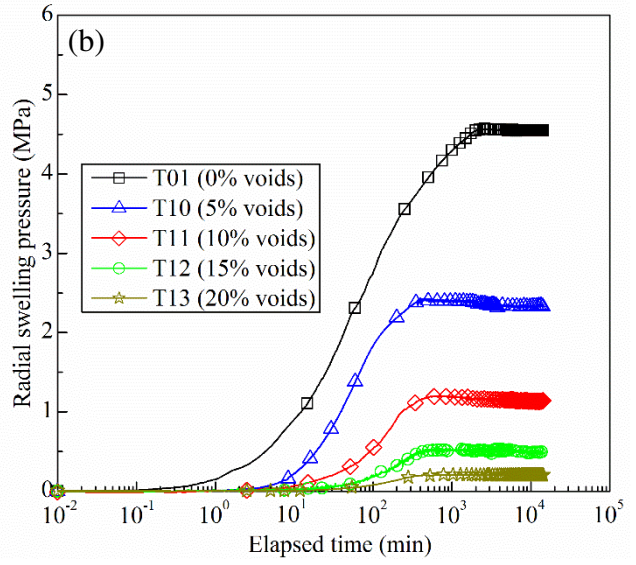
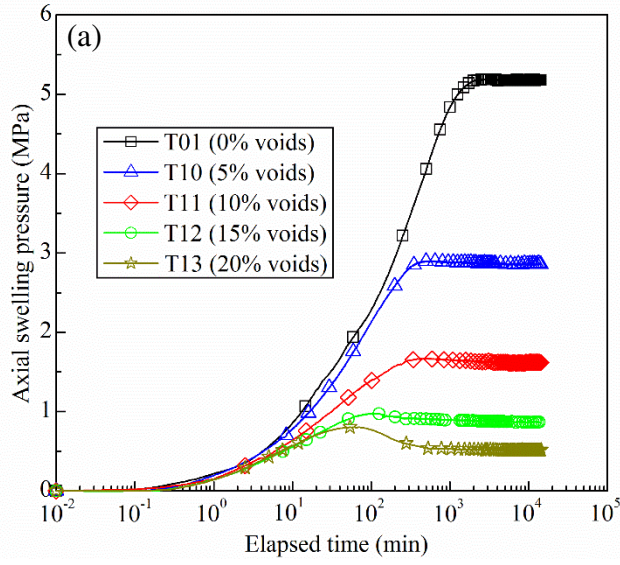
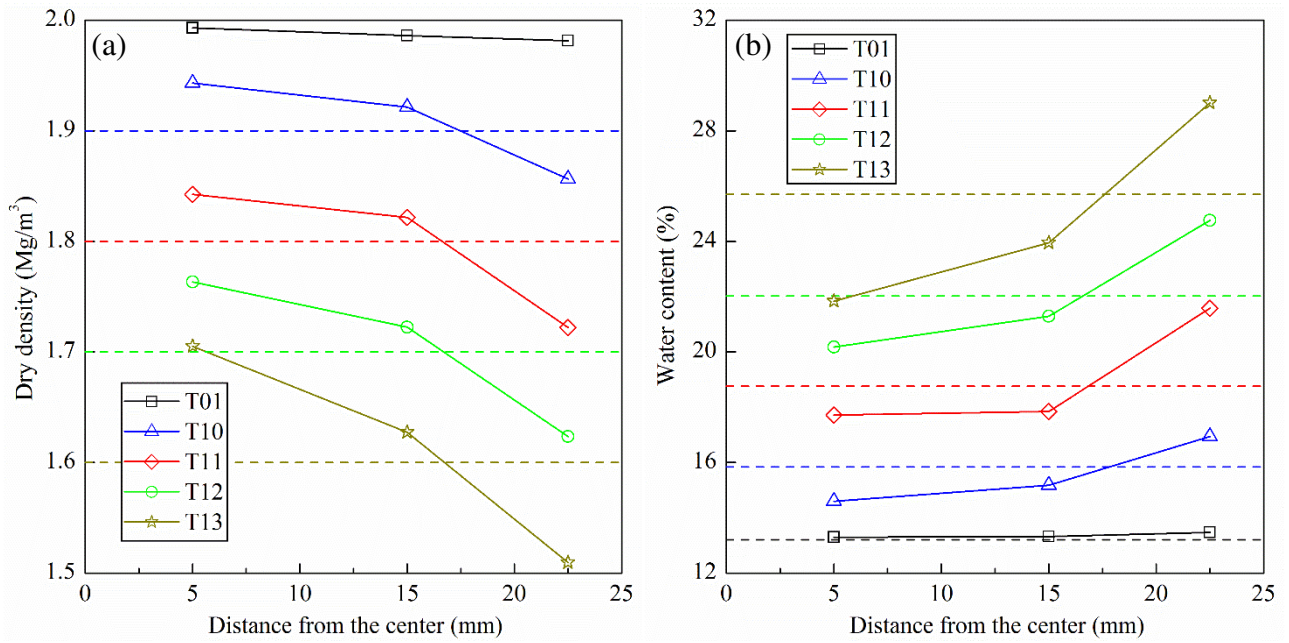


Fig. 8 Evolutions of axial and radial swelling pressures of samples with radial voids: (a) axial swelling pressure and (b) radial swelling pressure

594
595
596



597
 598
 599
 600
 601

Fig. 9 Dry density and water content profiles for sample T01 and those with radial voids (T10 to T13): (a) dry density and (b) water content. Note: the dash lines in the left graph represent the global dry density calculated using the total volume after filling technological voids instead of initial state while the dash lines in the right graph refer to the global water content corresponding to the global dry density and a 100% degree of saturation

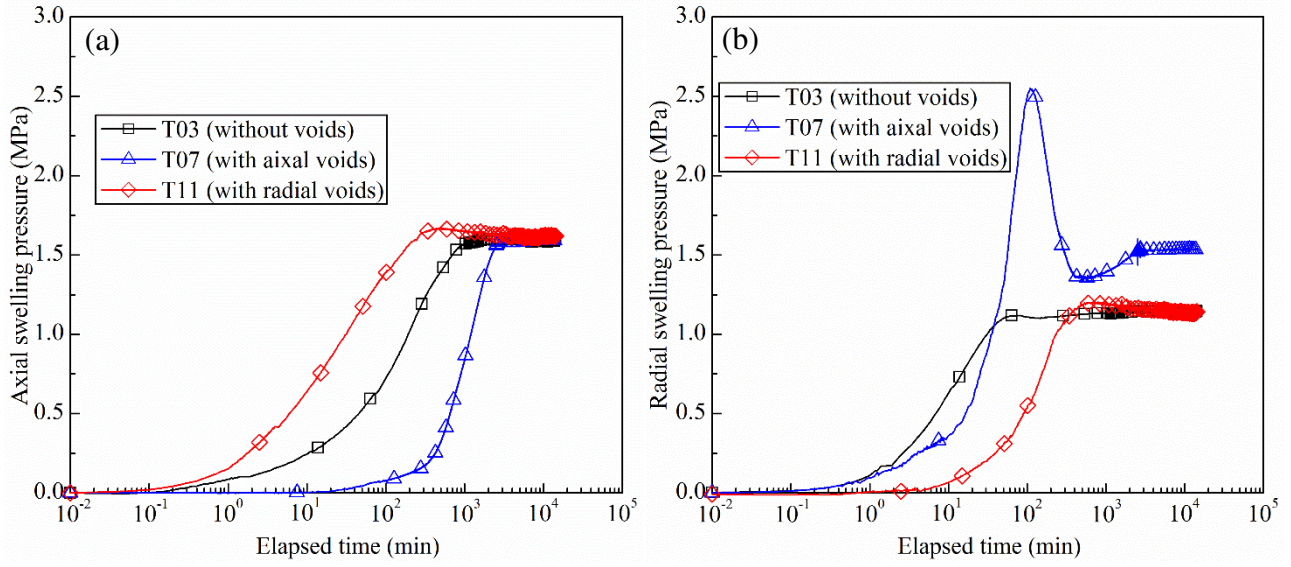
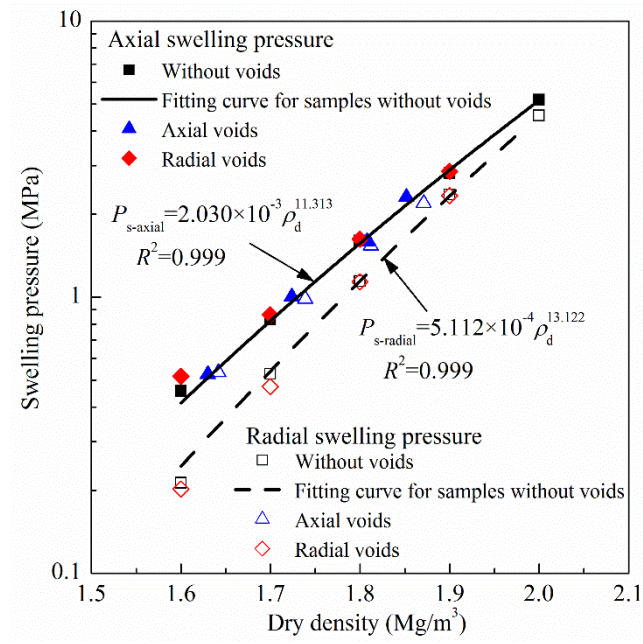


Fig. 10 Comparison of the swelling pressure kinetics of samples in different cases: (a) axial swelling pressure and (b) radial swelling pressure

602
603
604

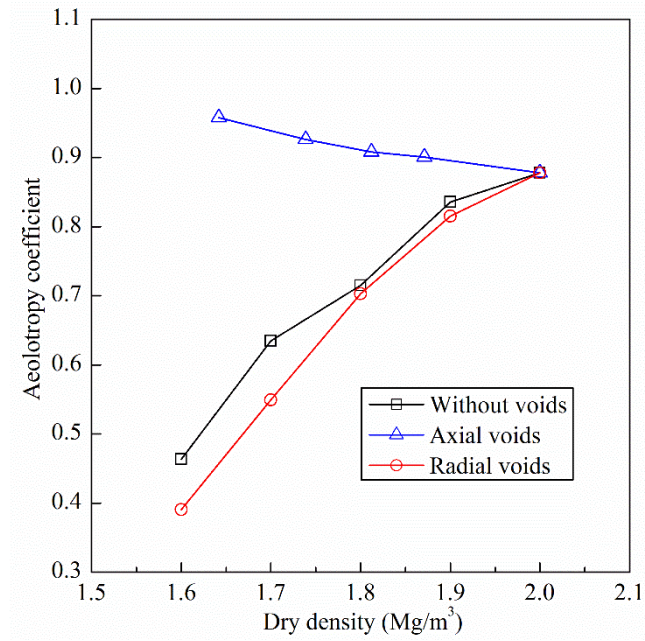
605



606

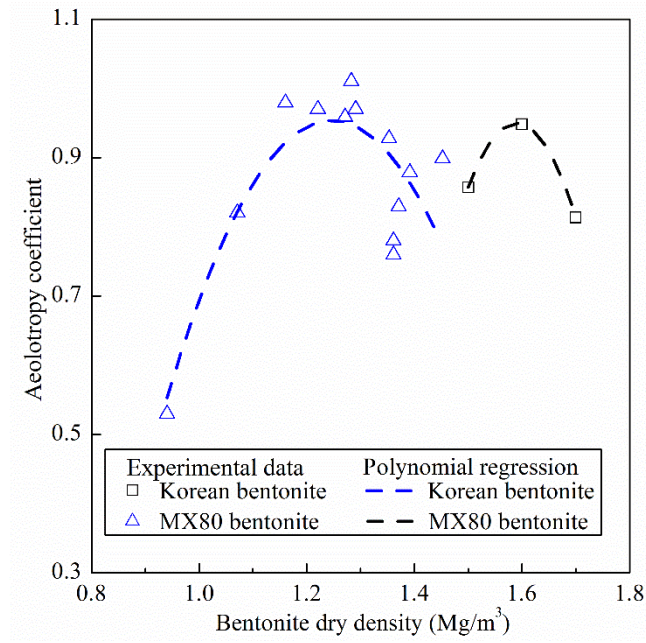
607

Fig. 11 Relationship between axial and radial swelling pressures and dry density



608
 609
 610
 611

Fig. 12 Relationship between aelotropy coefficient and dry density of bentonite/claystone mixture. Note: the aelotropy coefficient of the samples with axial voids was determined according to the axial and radial swelling pressures of the soils in contact with the pressure sensor

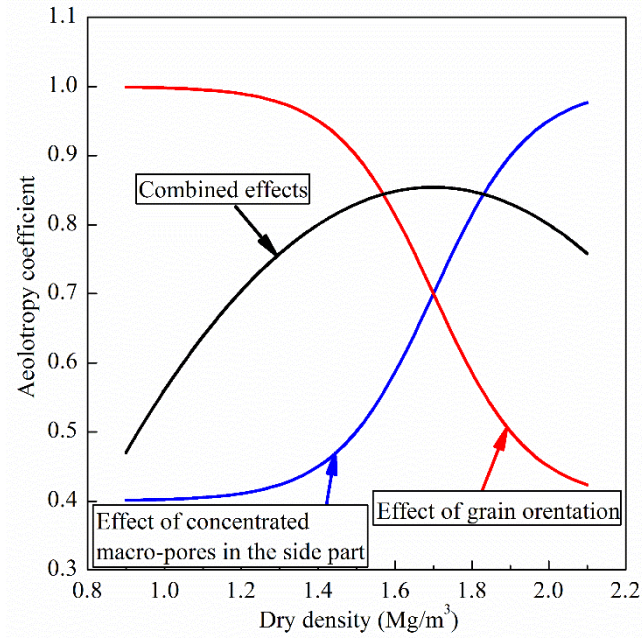


612

613

614

Fig. 13 Aeolotropy coefficient changes with bentonite dry density for different bentonites (data from [Lee et al. \(2012\)](#) and [Saba et al. \(2014a\)](#))



615

616

617

Fig. 14 Representation of the effects of grain orientation and concentrated macro-pores in the side part. Note: the curves in the figure are schematically drawn and do not represent measured values

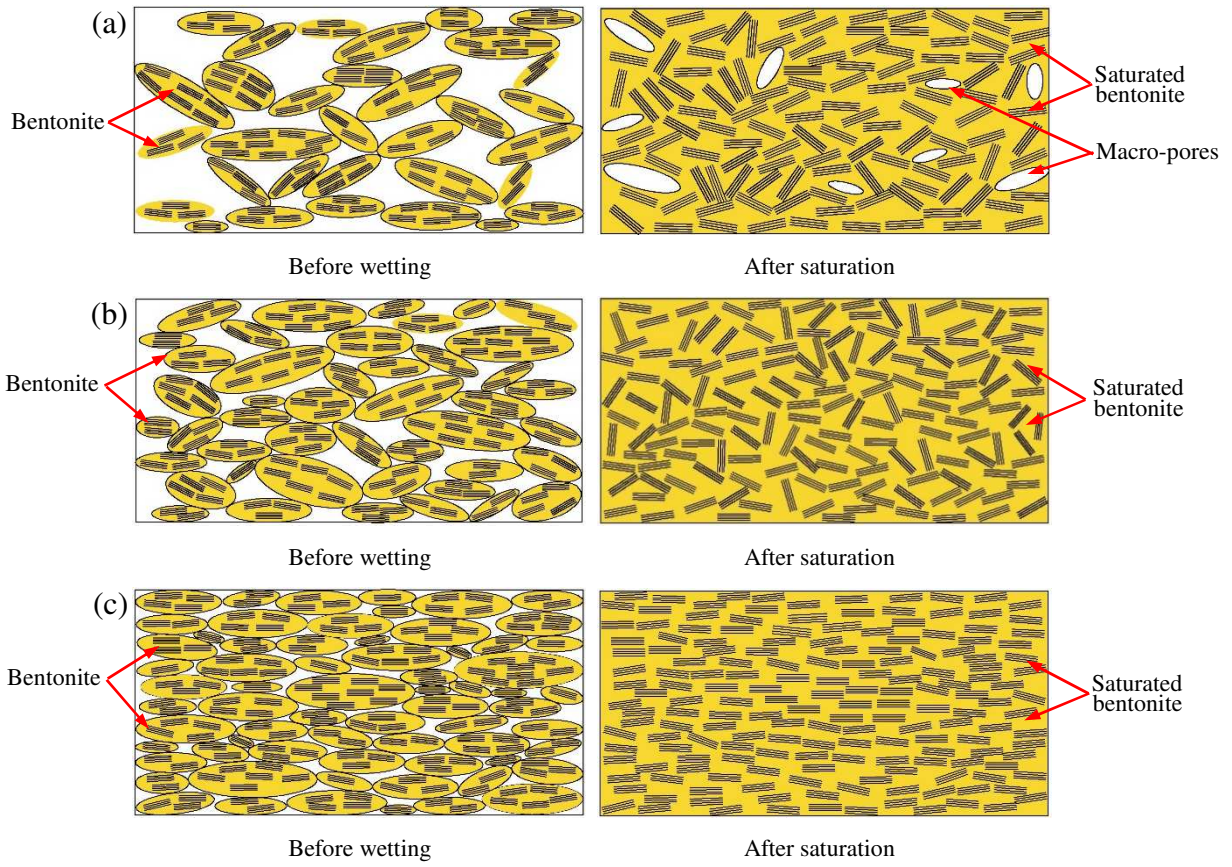


Fig. 15 Schematic view of aeolotropic swelling mechanism in compacted bentonite at: (a) low dry densities; (b) medium dry densities; (c) high dry densities

